Appl. Phys. B 74 [Suppl.], S127–S132 (2002)
DOI: 10.1007/s00340-002-0907-7

Applied Physics B
Lasers and Optics

M. ARMSTRONG[1]
P. PLACHTA[2]
E.A. PONOMAREV[2]
J.P. OGILVIE[2]
A.M. NAGY[2]
R.J.D. MILLER[2,✉]

Versatile seven-femtosecond pulse compressor of parametrically amplified pulses using adaptive optics: studies of the primary events in protein dynamics

[1] Department of Physics and Astronomy, University of Rochester, Rochester, NY 14627,USA
[2] Departments of Physics and Chemistry, University of Toronto, 80 St. George Street, Toronto, ON M5S 3H6, Canada

Received: 26 September 2001/
Revised version: 2 November 2001
Published online: 16 July 2002 •

ABSTRACT High-quality, few-cycle pulses over the complete tuning range of a noncollinear parametric amplifier system and a variety of sample conditions have been readily generated using a compressor based on deformable mirror adaptive optics. These broadband pulses are compressed to 7 fs pulse duration in a compact, glassless combination of static negatively chirped mirrors and a zero-dispersion stretcher with a deformable mirror for the manipulation of the spectral phase. These ultra-short pulses are then used to investigate with very high resolution the early-time dynamics of deoxy- and carboxymyoglobin after the photoinitiated dissociation of the carbon monoxide ligand.

PACS 42.65.Re; 82.20.Kh; 82.53.Eb

1 Introduction

Recently, it has been possible to attain few-cycle pulses that are of sufficiently short duration to impulsively drive and observe essentially all molecular modes in real time [1–3]. The phase of the vibrational periods reveals new information that is distinct from frequency-domain analogues and provides microscopic details of the time evolution of molecular wavefunctions. It is most useful to have a tunable source for these ultra-short pulses to permit tuning to the molecular states of interest, rather than being confined to certain molecular systems by the available laser fundamental and harmonics. Noncollinear optical parametric amplification (NOPA), in combination with various compressor schemes, has been employed to meet this objective and novel observations have been forthcoming. The previous approaches use either a series of prisms with small apex angles for phase-front correction [2, 4] or specifically designed chirped mirrors to compensate phase differences over a set central carrier wavelength [3]. Each approach has benefits over the other. The prism-compressor scheme is wavelength-agile and is able to compensate various degrees of dispersion introduced by the sample under study. The chirped-mirror approach is significantly easier to implement but is much less flexible. The present work represents a synthesis of the relative benefits of both approaches through the use of a deformable mirror–adaptive optics. The use of adaptive optics makes the system as flexible as the small apex prism approach with the possibility of correcting dispersion up to higher orders, while maintaining the same ease of implementation as with chirped mirrors.

✉ E-mail: dmiller@lphys.chem.utoronto.ca

2 Ultra-short visible-pulse generation and compression

For this work, the pulses were compressed and precompensated for material dispersion using a combination of chirped mirrors designed and manufactured by R & D Laser Optics [5, 6] and a micromachined deformable mirror (DM) manufactured by OKO Technologies [7].

Ultra-broadband (> 50 nm bandwidth) pulses are generated using the optical setup illustrated in Fig. 1a. The NOPA is pumped by 120 fs, 350–400 μJ, 775 nm pulses at a repetition rate of 1 kHz from an all-diode-pumped, solid-state, chirped pulse amplification system with a doubled Er-doped fiber oscillator. White-light continuum is generated from a small portion of the pump (1–2 μJ) in a 1 mm-thick sapphire crystal while the remaining pump is doubled in a 1 mm-thick BBO crystal to produce ∼ 150 fs, 75 μJ, 388 nm pulses. Amplification of the white-light seed pulse to greater than 5 μJ (with $M^2 < 1.2$ beam quality) via the NOPA process with 75 μJ of doubled pump light takes place in a 1 mm-thick BBO crystal cut for type I doubling. This amplified white light is then collimated and compressed using the scheme shown in Fig. 1b. A pair of high-reflectivity chirped mirrors which impart approximately $-40\,\mathrm{fs}^2$ of group delay dispersion (GDD) per bounce between 500–650 nm are used to precompensate the pulses. The pulses are then further compressed by a computer-controlled deformable mirror in the Fourier plane of a 30 cm zero-dispersion stretcher [8]. The output pulses have < 5% peak to peak energy fluctuations and < 5% drift over an hour of operation. A typical spectrum is shown in Fig. 2. Although it is possible to generate much broader bandwidths, we only obtained 1–2 μJ pulse energy with bandwidths greater than 80 nm.

The DM consists of a gold-coated silicon nitride membrane suspended over 39 electrostatic actuators arranged in a 3×13 rectangular array. Independently assigned discrete voltages between 0 and 250 V (8 bit resolution) are applied

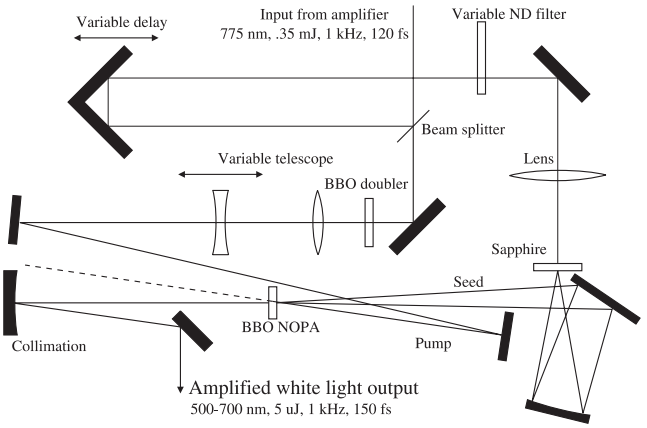

a Noncollinear OPA

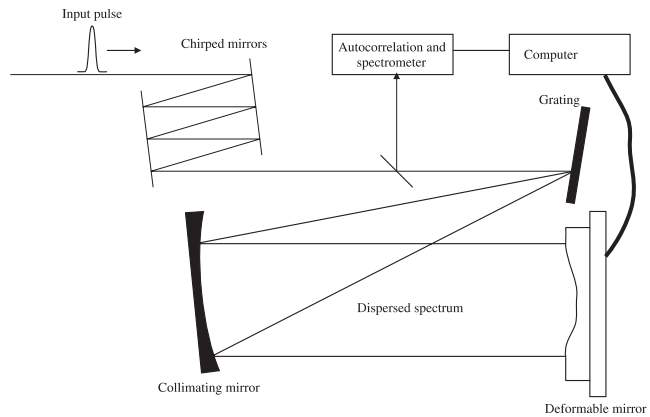

b Compression scheme

FIGURE 1 Schematic of the noncollinear optical parametric oscillator (NOPA) and compressor layout

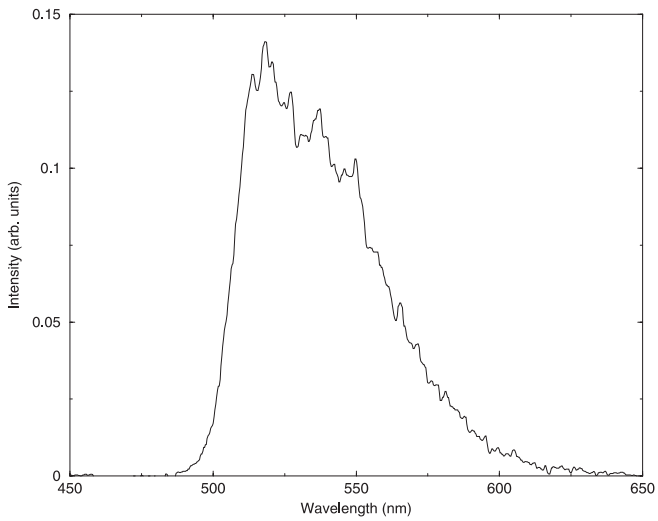

FIGURE 2 Pulse spectrum with a FWHM frequency bandwidth of about 53.4 THz

to the actuators to deflect the mirror. The continuous nature of the membrane yields a smooth mirror profile, given by the convolution of an influence function over the actuator voltages. The advantage of this type of phase modulation is that, in contrast to liquid-crystal phase modulators, it has no dead space and the imparted phase profile will be continuous, rather than a set of discrete steps.

Previously, a similar deformable mirror was used to compensate as much as 1 cm of material for near-time–bandwidth-limited 15 fs pulses [9] in the near IR of an amplified Ti:sapphire system. For this work, significantly shorter pulses were required. The combination of chirped mirrors and adaptive optics provides a material-free programmable compensation system that is compact. In addition, after the initial alignment, the adjustment for optimum compression is possible via computer control of the deformable mirror with a simple, fast search algorithm.

To optimize the pulse duration, a second harmonic is generated in a 20 μm-thick type II BBO doubling crystal using light from one arm of the autocorrelator. A computerized genetic learning algorithm varies the mirror profile while monitoring the generated second harmonic to determine the optimum mirror configuration for a particular amount of dispersion. Although the algorithm may optimize by varying every actuator independently, this search involves a very large parameter space (256^{13} mirror profiles). In reducing the number of degrees of freedom by expanding the actuator potentials in polynomial orders with as few as three degrees of freedom (second-order polynomial), the mirror configuration for the optimized short pulse can be found in < 1 min. Although alignment of the zero-dispersion stretcher is critical, precise knowledge of the mirror deformation and the resulting phase profile is difficult to determine theoretically [9]. Nevertheless, even without detailed knowledge of the phase of the input pulse or the phase dispersion profile through the DM/zero-dispersion stretcher, successful pulse compression is achieved using this technique. Complete experimental details have been previously outlined [10].

Full characterization of the time-dependent amplitude and phase of the laser pulse is possible with either FROG (frequency-resolved optical gating) or SPIDER (spectral interferometry for direct electric-field reconstruction). This information can be used in turn as an input to the deformable mirror for full optimization. Second harmonic generation (SHG) FROG was carried out on the broadband amplified pulses from the OPA; however, low signal levels of the second-harmonic frequencies in the UV made the signal acquisition times too long to be useful to the optimization process. Currently, a form of transient grating FROG, which makes use of third-order nonlinear processes, is being implemented to detect the signal in the visible, eliminating the limitations observed with UV detection. In addition, by using a BOXCARS beam geometry commonly used in four-wave-mixing experiments, the FROG signal is background-free, and the beams are automatically phase-matched.

In the absence of a sufficiently fast FROG input, we have relied on the intensity of the second harmonic as the input signal and interferometric autocorrelation for compatibility.

A representative interferometric autocorrelation of the compressed pulse is shown in Fig. 3. This autocorrelation was obtained after the pulse had traversed 3 mm of fused silica, approximately the amount in the interferometer and sample-cell window of our experiment. It has been shown by Naganuma et al. that the spectrum and interferometric autocorrelation can uniquely determine the amplitude and phase distribution of

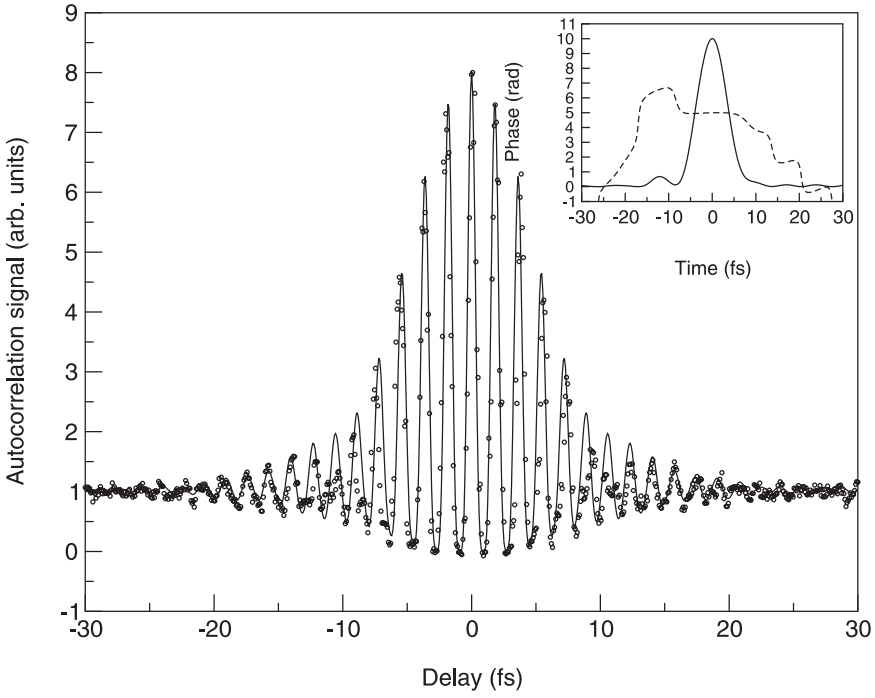

FIGURE 3 Autocorrelation of the compressed pulses (*points*) and fit (*solid line*) from the pulse recovery. The *upper right* shows the temporal amplitude envelope (*solid line*) and phase (*dashed line*) derived from the interferometric autocorrelation using the method of Peatross and Rundquist [11]

a pulse [12]. Although direct characterization of pulse amplitude and phase using empirical diagnostics is preferable to numerical methods, these may still give an indication of the pulse intensity and phase profiles. Recently, Peatross and Rundquist [11] developed an iterative method (temporal information via intensity, or TIVI) to determine the intensity distribution from an intensity autocorrelation (which may be derived from the interferometric autocorrelation). Along with the pulse spectrum, the resulting intensity–time distribution derived from TIVI may be used as an input to the Gerchberg–Saxton algorithm [13] to determine the phase profile of the pulse.

The results of this analysis are shown in the inset of Fig. 3. Assuming a Gaussian pulse, with a deconvolution factor of 1.41, the width of the interferometrically derived intensity autocorrelation is 9.2 fs (all measurements have an error of $\pm 5\%$), giving a pulse full width at half maximum of 6.6 fs. In comparison, the TIVI algorithm results in a temporal intensity FWHM of 6.7 fs. The output from the Gerchberg–Saxton algorithm using the TIVI result is shown in Fig. 3. As can be seen, wings present on the intensity profile are less than 10% of the central peak intensity, and over the region of significant pulse intensity, the resulting phase is quite linear.

As a check of the relative quality of the inferred phase shape, the fit to the interferometric autocorrelation assuming the generated phase and intensity profile is shown as the solid line through the data. The FWHM of the derived intensity profile from this procedure is 7.7 fs and, given the relative accuracy, is consistent with the interferometric measurement. For comparison, assuming a linear phase across the spectrum, the FWHM pulse width would be 6.2 fs.

The pump–probe cross correlation was measured by replacing the sample in a standard small-angle noncollinear pump–probe configuration with a BBO autocorrelation crystal. A pulse width of between 7 and 8 fs at the start of the sample is confirmed from the second-harmonic intensity cross correlation. This methodology has also been applied to the optically initiated photodissociation processes in myoglobin (Mb), as will be described below.

3 Pump–probe experiments

In the interest of investigating the detailed early-time dynamics of the heme in myoglobin after a photodissociation event, pump–probe data were obtained for carboxy- (MbCO) and deoxymyoglobin (deoxyMb). In this case, the probe was spectrally dispersed and detected at 538 nm. Results obtained at other wavelengths did not provide qualitatively different information and generally had inferior signal to noise. Both pump and probe were identical with a typical spectrum shown in Fig. 2. The monochromator resolution for dispersed detection was 2 nm and the probe was detected using a typical reverse-bias photodiode. The modulated probe signal was detected using a Stanford Research SRS530 lock-in detector, and a Melles Griot Nanostep delay stage with better than 100 nm absolute accuracy in positioning was used for the delay line. All data sets were obtained as the average of 20–30 actual scans.

Both MbCO and deoxyMb samples were prepared starting with horse heart met (unreduced) myoglobin from Sigma-Aldrich dissolved in 0.2 M TRIS buffer (0.1 M NaCl and 1 mM EDTA) adjusted for a pH of 7.0. Carbon monoxide (for MbCO) or molecular nitrogen (for deoxyMb) was flowed over the sealed sample for two hours (in the case of CO) or overnight (in the case of N_2), removing oxygen dissolved in the buffer and replacing it with the desired ligand (or lack of one). The sample was then reduced using a two-fold excess (per mole of sample) of sodium dithionite. At this stage, the heme bonds with the nearest appropriate ligand, CO in the case of MbCO and no ligand in the case of deoxyMb. Sam-

ples were continuously degassed during all experiments and all tubing was rigorously sealed to prevent oxygen contamination. Since the time required for a CO ligand to recombine with the protein is comparable to the delay between laser shots, all samples were flowed to ensure a fresh sample volume for a given pump–probe pair.

Typical raw MbCO data obtained at 538 nm and its linear predictive singular value decomposition (LPSVD) fit and residual [14, 15] are shown in Fig. 4. The inset to Fig. 4 shows the entire pump–probe trace including pump–probe data for time delays with $t_{\text{delay}} = t_{\text{probe}} - t_{\text{pump}} \leq 0$. Notable is the contribution to the signal from the glass. Typically for nonresonant nonlinear index of refraction (n_2) effects [16], one would only expect a signal when the pump and probe overlap [17]. Thus, a signal outside the pump–probe overlap region (as shown by the autocorrelation) indicates either resonant higher-order population dynamics of the window material or n_2 effects between longer pulses. In this case, we observed no qualitative variation of the glass signal with material, likely indicating that the coherent spike at $t = 0$ was due to the nonlinear index of refraction, not population dynamics. This indicates that the pulse was negatively and positively chirped at the entrance and exit windows, respectively. Still, the pulse width indicated by cross correlation is consistent with a sub-10 fs pulse at the sample position. Although this window contribution to the signal clouds the early-time dynamics, the time resolution of the measurement for delays greater than 50 fs is consistent with an 8 to 12 fs pulse, based on the vibration frequencies modulating the signal. Zero pulse delay is located using the glass signal, which can be con-

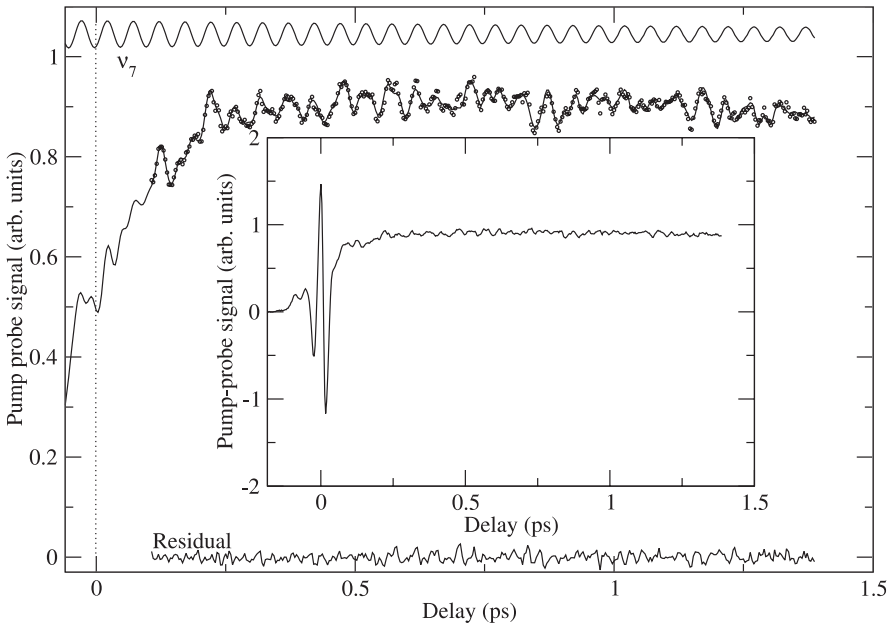

FIGURE 4 Pump–probe signal of MbCO at 538 nm with linear predictive singular value decomposition fit. The *inset* shows the entire pump–probe trace including delays with $t_{\text{delay}} \leq 0$. The portion of the signal due to the ν_7 mode is shown as the *uppermost curve*

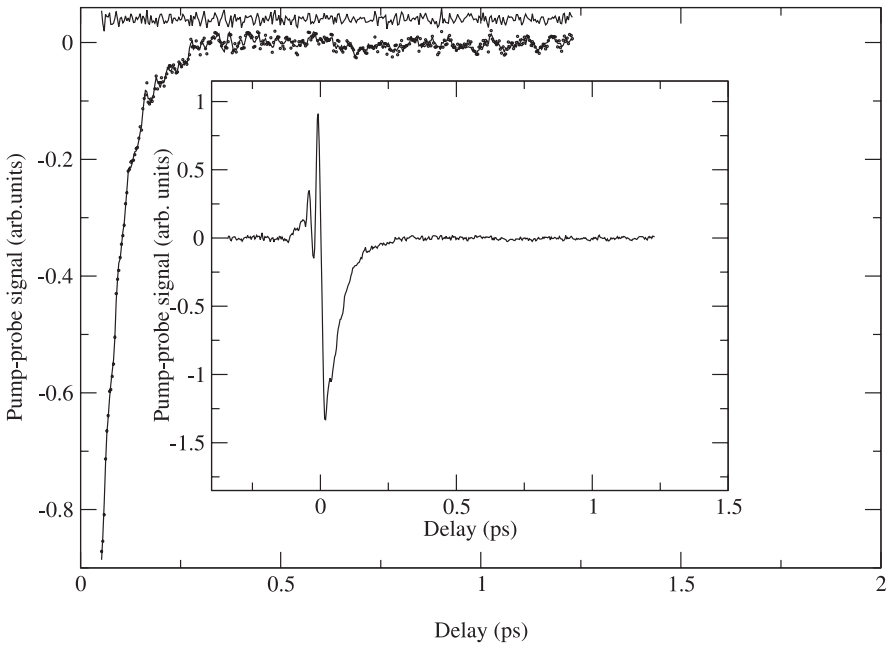

FIGURE 5 Pump–probe signal of deoxyMb with probe detection at 538 nm and *inset* with delays such that $t_{\text{delay}} \leq 0$, as per Fig. 4

sistently located with respect to the autocorrelation trace to within ±3 fs of delay.

Typical raw deoxyMb data obtained at 538 nm (along with LPSVD fit and residual) are shown in Fig. 5 (with the inset to this figure showing the entire pump–probe trace). All deoxy samples were prepared to give the equivalent absorption (50%–80%) to MbCO samples. Although these data do not extend in time beyond 1.5 ps, within this regime they are consistent with other measurements of the ground-state vibrational relaxation of deoxyMb [18]. Most notable in this data is the absence of strong oscillation at any frequency, with even the strongest mode (the ν_7 mode) [18–20] having nearly five times smaller amplitude in deoxyMb than in MbCO relative to the baseline population dynamics. Since the electronic structure of deoxyMb is significantly perturbed with respect to MbCO, the reduction in the amplitude of these oscillations (adjusted for absorption) is not necessarily an indication that oscillations in MbCO are due to photolysis of the CO. Indeed, given the significant perturbation to the transmission even with small levels of bleach, it would be very challenging to obtain true control data for the contribution to the signal due to unphotolyzed, Raman-excited ground-state MbCO (with excitation in the Q-band), which would require a calibrated comparison of high-bleach and low-bleach experiments with signal differences far below the signal to noise obtained in these studies. This distinction is made based on the frequency modulations for the MbCO case.

4 Data analysis and discussion

All time traces were normalized with respect to both pump and probe energies. An illustration of the ν_7 portion of the MbCO signal is shown in Fig. 4. Generally, the most notable distinction between the MbCO and deoxyMb data sets is the relative strength of the oscillations found in MbCO, typically found to be 3–5 times stronger than their counterparts in deoxyMb. Since the equilibrium resonance Raman data of MbCO and deoxyMb are not different in intensity by more than 50% (see below), this is an indication that resonance Raman excitation processes are not responsible for the observed modulated signal. From this information, we infer that the observed oscillations are due to the pump-induced chemical reaction, while Raman-driven processes are near the noise level of the detection. This conclusion is borne out by the fitted frequencies of the ν_4 and ν_7 modes.

As indicated by resonance Raman spectroscopy [20], the equilibrium frequencies of ν_7 and ν_4 for MbCO are 678 cm^{-1} and 1373 cm^{-1}, respectively, shifting to 676 cm^{-1} and 1355 cm^{-1} in the deoxy species. The ν_7 oscillation is clearly the most significant contribution to the MbCO time-domain signals in this study. Due to the absorptive $\chi^{(1)}$ character of the probe interaction in the well-separated-pulse limit [21], the traces shown here are only sensitive to pump-induced wavepacket motion. Therefore, what is observed must be due to either Raman-excited modes of unphotolyzed MbCO (which would still have the MbCO ground-state energy of 678 cm^{-1}), or photolysis-induced wavepacket motion. Since the quantum yield of dissociation upon photon absorption is 100%, these possibilities are mutually exclusive for a given molecule. If a pump photon is absorbed, then wavepacket motion must be due to the chemical reaction and, if no pump photon is absorbed to create an excited electronic state, then any wavepacket motion must be due to Raman-excited ground-state motion of MbCO. Yet, the energy of the oscillations that are observed is significantly shifted from the equilibrium MbCO peak, in the direction corresponding to the deoxy species (within the first picosecond), as observed by Mizutani and Kitagawa [20]. The fitted frequencies of ν_7 in all recorded MbCO pump–probe time traces have an average of $670 \pm 3.6\,cm^{-1}$. This indicates that ν_7 in the carboxyMb samples corresponds (at least in part) to an oscillation in just deligated deoxyMb. Fourier-transform analyses (including deconvolution due to the finite pulse width) of the time traces also put the ν_7 energy about 10 cm^{-1} below the equilibrium MbCO peak, although the Fourier transform does not have sufficient resolution to resolve the precise frequency of oscillations. Although the actual signal will be due to some mixture of different molecules that either dissociated or Raman scattered, there are accompanying experimental observations that favor the reaction-driven case. That is, the magnitude of the shift (even beyond the equilibrium deoxyMb energy), and the absence of a significant Raman signal in deoxyMb combined with equilibrium Raman spectra (that show no observable Raman scattering for ν_7 in the deoxy- and carboxyMb forms), are supporting evidence that ground-state motion in the photoinduced deoxyMb is the more significant contributor to the total signal. Although pump-induced field-driven background should be present in these studies, there is no contribution analogous to static Raman scattering present in transient Raman experiments. Similar comments are true for oscillations at ν_4, with the post-ligation vibrational energy significantly shifted toward the equilibrium deoxyMb value. Relative to the total observed shift between equilibrium MbCO and deoxyMb, ν_4 is not as strongly shifted as ν_7, being about 5 cm^{-1} above the observed equilibrium deoxyMb energy. This is most likely due to more significant presence of Raman-scattered ground-state MbCO dynamics or an incomplete shift due to the early time of the measurement. Nonetheless, this large shift is, again, a strong indication that chemical reaction induced dynamics are a dominant portion of the total signal.

The experimentally derived phase of the ν_7 oscillation at 538 nm detection wavelength is -160 ± 30 degrees. The phase of the actual physical vibration will be ambiguous, with a possible 180 degree phase shift [21, 22], putting the actual phase of the vibrational motion at -160 degrees or 20 degrees. Using the method of Champion and co-workers [21], we calculate the phase for field-induced Raman excitation of the ground state of MbCO to be 80 degrees (with the same 180 degree ambiguity). Within the experimental error, this is inconsistent with the measured phase and provides additional evidence that the observed oscillation is due to chemical reaction induced wavepacket motion. Assuming the reaction does not occur at $t = 0$, the measured phase puts the chemical reaction crossing point at 30 ± 5 fs after the creation of the photoexcited wavepacket of MbCO.

5 Summary

The development of convenient, stable sources of sub-10 fs pulses has enabled the study of the very fast dynam-

ics of myoglobin in the first instant after a photon-initiated chemical event. Unlike previous transient resonance Raman studies [20], these measurements provide a more comprehensive window into the early-time dynamics of a reactive system through direct observation of wavepacket motion via the molecular dipole moment. Since pump–probe measurements are only sensitive to actual wavepacket motion (as opposed to Stokes Raman measurements, which probe the vibrational structure of the entire sample, including unexcited molecules), pulse measurements can chart the actual progress of the wavepacket through the chemical reaction crossing point. Although this study was ultimately limited by signal to noise (with the relatively low differential absorption levels available with excitation in the Q-band) and dispersion issues, compelling evidence has been presented of strong chemical reaction induced oscillations in the heme of myoglobin in the first instants (< 10 fs) after the pump-induced creation of an excited state of MbCO, with a measurement of the phase of those oscillations that is unavailable from Raman measurements. These measurements provide direct evidence that the excited-state wavepacket of MbCO is strongly channeled into ν_7 and ν_4 oscillations of the heme in ground-state deoxyMb photoproduct, with phases that are consistent with a very fast reaction rate and/or a small potential difference between the excited-state wavepacket and the chemical reaction crossing point. This, in turn, is indicative of coupling between the deformation of the heme upon dissociation of the ligand and the completely symmetric in-plane oscillations of ν_7 and ν_4. In this regard, we are now able to directly observe the nuclear motions involved in the transition-state crossing in a chemical reaction of a condensed-phase system. The elucidation of this mechanism and its relation to the primary events which direct biological processes has been a long standing goal. It has been possible to gain these new insights through the development of amplified few-cycle pulses that can be optimized using adaptive optics for a wide variety of sample conditions.

ACKNOWLEDGEMENTS We thank the Natural Sciences and Engineering Research Council of Canada and Photonics Research Ontario for funding this work.

REFERENCES

1 G.M. Gale, M. Cavallari, F. Hache: J. Opt. Soc. Am. B **15**, 702 (1998)
2 T. Kobayashi, A. Shirakawa: Appl. Phys. B **70**, S239 (2000)
3 G. Cerullo, M. Nisoli, S. Stagira, S. De Silvestri: Opt. Lett. **23**, 1283 (1998)
4 A. Shirakawa, I. Sakane, M. Takasaka, T. Kobayashi: Appl. Phys. Lett. **74**, 2268 (1999)
5 R. Szipocs, A. Kohazi Kis: Appl. Phys. B **65**, 115 (1997)
6 A. Stingl, C. Spielmann, F. Krausz, R. Szipocs: Opt. Lett. **19**, 204 (1994)
7 G. Vdovin, S. Middelhoek, P.M. Sarro: Opt. Eng. **36**, 1382 (1997)
8 O.E. Martinez: IEEE J. Quantum Electron. **QE-23**, 1385 (1987)
9 E. Zeek, K. Maginnis, S. Backus, U. Russek, M. Murnane, G. Mourou, H. Kapteyn: Opt. Lett. **24**, 493 (1999)
10 M.R. Armstrong, P. Plachta, E.A. Ponomarev, R.J.D. Miller: Opt. Lett. **26**, 1152 (2001)
11 J. Peatross, A. Rundquist: J. Opt. Soc. Am. B **15**, 216 (1998)
12 K. Naganuma, K. Mogi, H. Yamada: IEEE J. Quantum Electron. **QE-25**, 1225 (1989)
13 R.W. Gerchberg, W.O. Saxton: Optik **35**, 237 (1972)
14 R. Kumaresan, D.W. Tufts: IEEE Trans. Acoust. Speech Signal Proc. **30**, 833 (1982)
15 F. Rosca, A.T.N. Kumar, X. Ye, T. Sjodin, A.A. Demidov, P.M. Champion: J. Phys. Chem. **104**, 4280 (2000)
16 A.A. Siegman: *Lasers* (University Science Books, Mill Valley, CA 1986)
17 S.L. Palfrey, T.F. Heinz: J. Opt. Soc. Am. B **2**, 674 (1985)
18 Y. Kholodenko, M. Volk, E. Gooding, R.M. Hochstrasser: Chem. Phys. **259**, 71 (2000)
19 M. Abe, T. Kitagawa, Y. Kyogoku: J. Chem. Phys. **69**, 4526 (1978)
20 Y. Mizutani, T. Kitagawa: Science **278**, 443 (1997)
21 A.T.N. Kumar, F. Rosca, A. Widom, P.M. Champion: J. Chem. Phys. **114**, 701 (2001)
22 A.T.N. Kumar, F. Rosca, A. Widom, P.M. Champion: J. Chem. Phys. **114**, 6795 (2001)